



ELSEVIER

Nuclear Physics A 648 (1999) 263–279

NUCLEAR  
PHYSICS A

## $\Sigma^+ p$ elastic scattering in the region of $300 \leq p_\Sigma \leq 600$ MeV/c with a scintillating fiber target

J.K. Ahn<sup>a,1</sup>, B. Bassalleck<sup>b</sup>, M.S. Chung<sup>c</sup>, W.M. Chung<sup>d</sup>, H. En'yo<sup>c</sup>,  
T. Fukuda<sup>e</sup>, H. Funahashi<sup>c</sup>, Y. Goto<sup>c,2</sup>, A. Higashi<sup>e,3</sup>, M. Ieiri<sup>f</sup>,  
M. Inuma<sup>c</sup>, K. Imai<sup>c</sup>, Y. Itow<sup>c,4</sup>, H. Kanda<sup>c</sup>, Y.D. Kim<sup>f,5</sup>, J.M. Lee<sup>d</sup>,  
A. Masaïke<sup>c</sup>, Y. Matsuda<sup>c</sup>, S. Mihara<sup>c,6</sup>, I.S. Park<sup>a</sup>, Y.M. Park<sup>g</sup>,  
N. Saito<sup>c,2</sup>, Y.M. Shin<sup>h,i</sup>, K.S. Sim<sup>a</sup>, R. Susukita<sup>c,2</sup>, R. Takashima<sup>j</sup>,  
F. Takeuchi<sup>k</sup>, P. Tlustý<sup>e,7,8</sup>, S. Yamashita<sup>c,6</sup>, S. Yokkaichi<sup>c</sup>,  
M. Yoshida<sup>c,2</sup>

### KEK-PS E251 collaboration

<sup>a</sup> Department of Physics, Korea University, Seoul 136-701, Korea

<sup>b</sup> Department of Physics, University of New Mexico, N.M. 87131, U.S.A.

<sup>c</sup> Department of Physics, Kyoto University, Kyoto 606-01, Japan

<sup>d</sup> Department of Physics, Yonsei University, Seoul 120-749, Korea

<sup>e</sup> Institute for Nuclear Study, University of Tokyo, Tanashi, Tokyo 188, Japan

<sup>f</sup> KEK, High Energy Accelerator Research Organization, Tsukuba 305, Japan

<sup>g</sup> Department of Physics, Kyungshung University, Pusan 608-736, Korea

<sup>h</sup> Department of Physics, University of Saskatchewan, Saskatoon, Saskatchewan, Canada

<sup>i</sup> Department of Physics, Seoul National University, Seoul 151-742, Korea

<sup>j</sup> Kyoto University of Education, Kyoto 612, Japan

<sup>k</sup> Department of Physics, Kyoto Sangyo University, Kyoto 603, Japan

Received 3 March 1998; revised 25 January 1999; accepted 1 February 1999

### Abstract

$\Sigma^+ p$  elastic scattering has been studied using a scintillating fiber block (SCIFI) which served as a target for the production of  $\Sigma^+$  hyperons as well as for subsequent  $\Sigma^+$  scattering on hydrogen. A new technique for the analysis of the hyperon–nucleon scattering in the SCIFI has been developed and established. In this paper,  $\Sigma^+ p$  elastic scattering events have been identified in the  $\Sigma^+$  momentum range of 300–600 MeV/c, and differential cross sections have been obtained at two angles. The results are compared with various theoretical baryon–baryon interaction models.

© 1999 Elsevier Science B.V.

PACS: 13.75.Ev; 21.30.Cb; 25.60.Bx; 25.80.Pw

Keywords:  $\Sigma^+p$  elastic scattering; Hyperon-nucleon interaction; Differential cross sections; Scintillating fiber block target

---

## 1. Introduction

Studies of baryon–baryon (BB) scattering including hyperons are essential for the understanding of the strong interaction. In the non-strangeness sector, nucleon–nucleon (NN) scattering has been studied quite extensively, and abundant data on differential and total cross sections, and spin observables for NN scattering exist in a wide range of incident nucleon energies. Theoretically, the NN scattering data are well described by one boson exchange (OBE) models.

However, there are not many experimental data on hyperon–nucleon (YN) scattering, especially in the low energy region. The existing data are from bubble chamber experiments performed in the 1960's [1]. Among many difficulties in obtaining experimental data on YN scattering the major one arises from the short lifetime of hyperons which demands that the hyperon production target must also serve as the scattering target in the low energy region. Despite the scarcity of experimental data, reasonable progress has been made toward the understanding of the YN interaction.

The OBE models developed for NN scattering have been extended to YN scattering by the Nijmegen group and the Bonn–Jülich group. The former extended their NN interaction model to include YN interactions using the flavor SU(3) symmetry [2], while the latter developed a model based on the SU(6) symmetry [3]. These models based on OBE potentials were tuned to reproduce the existing NN and YN scattering data, and parameters needed in the model are obtained from fits to the experimental data. However, due to the scarcity of experimental data on YN channels, the parameters in these models are determined incompletely and are not fixed, and more experimental data are needed.

The study of YN scattering offers a unique way of probing the short range behaviour of BB interactions due to the added degree of freedom, the strangeness. Thus, it is desirable that the short-range repulsive force is described in a more fundamental manner. Since at short distances baryons overlap each other, their behaviour should be described with underlying degrees of freedom involving quarks and gluons. This problem is related to

---

<sup>1</sup> Present address: Department of Physics, Kyoto University, Kyoto 606-01, Japan.

<sup>2</sup> Present address: RIKEN, Institute of Physical and Chemical Research, Wako, Saitama 351-01, Japan.

<sup>3</sup> Present address: Public Health Department, Hyogo Prefectural Government, Kobe, Hyogo 650, Japan.

<sup>4</sup> Present address: Institute for Cosmic Ray Research, University of Tokyo, Tanashi, Tokyo 188, Japan.

<sup>5</sup> Present address: Department of Physics, Seoul National University, Seoul 151-742, Korea.

<sup>6</sup> Present address: International Center for Elementary Particle Physics, University of Tokyo, Tokyo 113, Japan.

<sup>7</sup> Permanent address: Nuclear Physics Institute of the Academy of Science, 250 68 Řež, Czech Republic.

<sup>8</sup> Present address: KEK, High Energy Accelerator Research Organization, Tsukuba 305, Japan.

the understanding of the non-perturbative regime of QCD. The groups from Tokyo [4], Tübingen [5] and Kyoto–Niigata [6] have independently approached the problem using the resonating group method (RGM) with antisymmetrized six-quark wave functions in the quark-cluster model (QCM).

We have undertaken a series of experimental investigations on YN scattering in order to provide new experimental data which should impose constraints on various models, and which help a better understanding of the strong interaction. As mentioned earlier, because of the short lifetime of hyperons the detector must be a production target for hyperons as well as their scattering target. Thus the detector must be capable of recognizing the three-dimensional complicated reaction sequence. To our knowledge, there are two such devices, nuclear emulsion and bubble chamber, both of which limit data rates severely. In order to overcome such a limitation, we have developed a new detector/target using scintillating fibers. In this paper, we present the first measurement of the cross section for  $\Sigma^+p$  elastic scattering by a new technology in the momentum region of  $\Sigma^+$ 's from 300 MeV/c to 600 MeV/c where no experimental data exist.

## 2. Experimental procedure

The experiment was performed at the K2 beam line of the 12-GeV Proton Synchrotron (PS) at KEK. A separated  $\pi^+$  beam was used to produce  $\Sigma^+$ 's through the ( $\pi^+$ ,  $K^+$ ) reaction, and subsequent scattering of the  $\Sigma^+$ 's was observed in a scintillating fiber (SCIFI) target. Fig. 1 shows the top view of the experimental setup consisting of the beam line, a spectrometer and the SCIFI target system. The system has been used in a previous  $H$ -dibaryon search experiment [7].

A 1.64 GeV/c  $\pi^+$  beam with  $\Delta p/p = 0.5\%$  (r.m.s.) and intensity of  $1 \times 10^5$  pions/spill ( $\sim 2$  s) was focused on the target. The beam particle identification was performed by measuring the time-of-flight between T1 and T2 scintillation counters with  $\Delta t = 85$  ps (r.m.s.), supplemented by the silica aerogel Čerenkov counter (BAC) and gas Čerenkov counter (GC). The particle momentum was measured by three sets of drift chambers (BDC1, BDC2 and BDC3) and two sets of multi-wire proportional chambers (BPC4 and BPC5). The contamination of  $e^+$ 's and  $\mu^+$ 's in the beam is  $\sim 7\%$ , and that of  $K^+$ 's and  $p$ 's is less than 1%.

The outgoing charged particles were momentum analyzed and detected with a spectrometer consisting of a dipole magnet (SP), drift chambers (DC1, DC2 and DC3), a cylindrical drift chamber (CDC), two sets of aerogel Čerenkov counters (FAC and SAC) and a TOF hodoscope (FTOF). The FAC and SAC vetoed scattered  $\pi^+$ 's. A coincidence matrix between the hodoscope (CH) in the entrance of the SP magnet and the FTOF counters was used for the first- and second-level trigger to provide approximate momentum information on the particle. The accepted momentum region by this coincidence matrix was from 650 MeV/c to 1450 MeV/c. The momentum of charged particles was determined using the CDC and DC's by the spline and the Runge–Kutta method in the off-line analysis. The momentum resolution ( $\Delta p/p$ ) was found to be

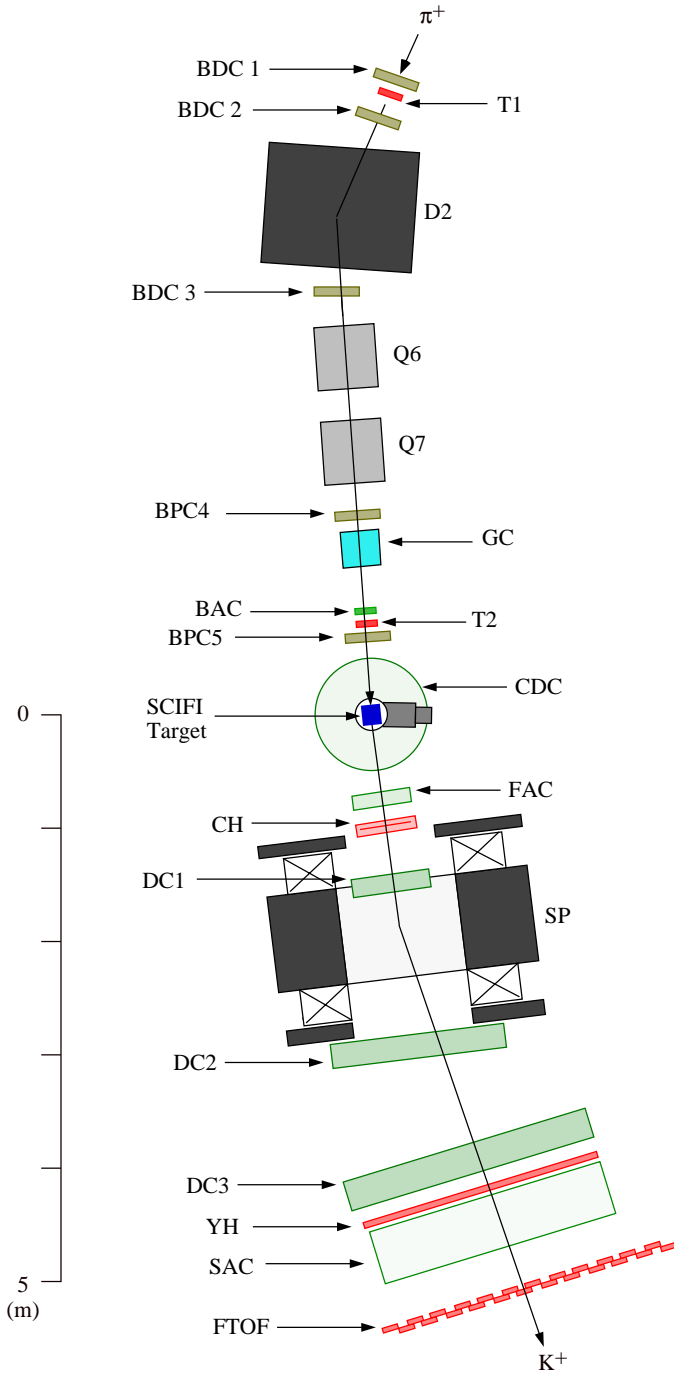


Fig. 1. Top view of the experimental setup.

0.9% (r.m.s.), where a tracking efficiency of wire chambers in the momentum determination procedure was 88%. The velocity was obtained from the flight path and the T2-FTOF time-of-flight information with  $\Delta t = 150$  ps (r.m.s.). Particles with mass between 400 and 600 MeV/ $c^2$  were chosen as  $K^+$ 's, where the background of  $\pi^+$ 's and p's was less than 0.4%. The tracking information from chambers in the beam line and the spectrometer was used in the automatic tracking process, which will be described later.

The scintillating fiber (SCIFI) target is a visual detector located at the focal point of the beam line. It consists of KURARAY SF81 plastic scintillating fibers [8], each of which has a  $500 \mu\text{m} \times 500 \mu\text{m}$  square cross section and is 20 cm long. The core size of the fiber is  $480 \mu\text{m} \times 480 \mu\text{m}$  square which is coated with 10- $\mu\text{m}$  thick cladding. The core material is polystyrene ((CH) $_n$ ) with refractive index of 1.59 and density of 1.06 g/cm $^3$ , while the cladding is made of polymethylmethacralate (PMMA, C $_5$ H $_8$ O $_2$ ) with  $n = 1.49$  and density of 1.18 g/cm $^3$ . The wavelength of induced scintillation photons is peaked at 437 nm.

Fig. 2 shows a schematic view of the SCIFI target. It was constructed in two stages; first 8 cm (width)  $\times$  20 cm (length) flat fiber sheets were constructed using 160 fibers for each sheet, then the sheets were stacked alternately in the vertical and horizontal direction. Each sheet was bonded to adjacent ones with black epoxy which also worked as an absorber to prevent the passage of light between the sheets. The average thickness of the glue was 50  $\mu\text{m}$ , and 92 such sheets in each direction were used to form a target volume of 8 cm (X)  $\times$  8 cm (Y)  $\times$  10 cm (Z). The space between the fiber sheets in each direction beyond the target volume created by stacking alternately was reduced from 550  $\mu\text{m}$  to 350  $\mu\text{m}$  at the readout arms in order to match the sensitive area of the image intensifier tubes (I.I.T.'s) which amplify the output light from the target. Two such I.I.T.'s (DELFT Model PP0040C) were used, one for the X-Z plane viewed from the vertical direction, and the other for the Y-Z plane viewed from the horizontal direction.

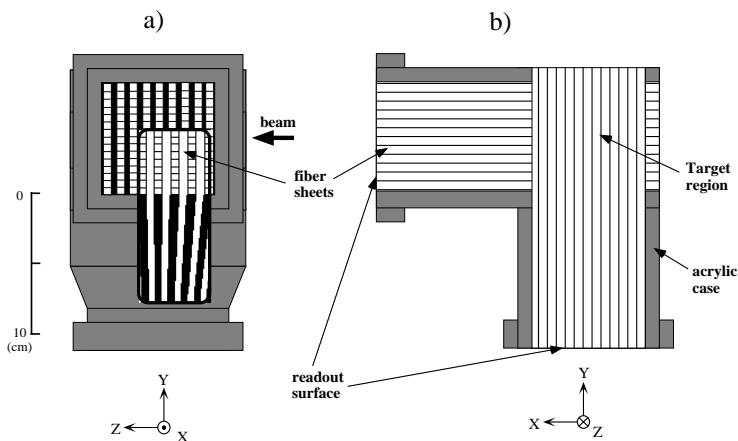


Fig. 2. Schematic view of the SCIFI target. a) view from the horizontal I.I.T. b) view from the upstream.

The DELFT I.I.T. is an assembly of three stages of independent image intensifiers. The first stage is an electrostatic type image intensifier with input and output windows 8 cm  $\varnothing$  and 1.8 cm  $\varnothing$ , respectively. The second and third stages are the same type using a micro-channel-plate (MCP) with a diameter of 1.8 cm. The first stage is operated in a DC mode with the cathode at 20 kV, and provides a light amplification factor of  $\sim 8$ . Since a phosphor with a short decay time is desired for the first stage to prevent overlapping of the triggered event and accidental events produced by particles in the beam arriving at the target earlier than the triggered event, P24 phosphor with a decay time of 2.4  $\mu\text{s}$  is used for the first stage. The phosphor for the second and third stages is P20 with decay time of 50  $\mu\text{s}$ . The amplification factor for each of the second and third stages was  $\sim 10^3$ .

The second stage of the I.I.T. was gated by the first-level trigger formed by  $\pi^+$ 's in the beam vetoed by scattered  $\pi^+$ 's within 400 ns after the interaction. The gate width was set at 2.5  $\mu\text{s}$  to prevent overlapping of the triggered events and accidental events produced by particles in the beam arriving later than the triggered event. The rate of the first-level trigger was 250/spill. The third stage was gated by a second level trigger, or mass trigger. The trigger was invoked within 15  $\mu\text{s}$  from the occurrence of the event with 1 ms gate width. The trigger was formed by the signal from the mass region of  $K^+$ 's in the "mass trigger" logic. The mass-trigger selection was determined by the momentum information given by the combination of the hit positions on CH and FTOF, and the time-of-flight information between T2 and FTOF counters obtained from the fast-encoding TDC modules. The trigger rate at this level was 16/spill.

The output (photon) images from the I.I.T. were viewed by a CCD camera (SONY XC-77) and recorded in the CCD chip containing  $768 \times 493$  pixels, the size of which is 8.8 mm  $\times$  6.6 mm with each pixel occupying 11  $\mu\text{m} \times 13 \mu\text{m}$ . The output video signal from the CCD camera was digitized in real time with a image digitizer. The pixel data had 32 bits which consisted of 10 bits and 9 bits for the two-dimensional coordinates, respectively, 7 bits for the brightness, and 6 bits for the event number.

Pinhole distortion effects of the SCIFI target system were investigated by utilizing the sheet structure of the SCIFI target. To find the optimum correction parameters, the position of each SCIFI sheet was identified by plotting the center of photon clusters, and the correction parameters were determined by making the sheet image straight. In this way the distortion effects were corrected up to first order. The position of each pixel in the real target was calibrated by placing on the SCIFI block aluminum plates with holes at predetermined positions and illuminating them with LED's.

Possible misalignment effects between SCIFI sheets, were checked with tracks left by incident  $\pi^+$ 's which should be straight lines. The mean value of the deviation of a hit position on each SCIFI sheet from the fitted straight line was attributed to the misalignment of the SCIFI sheet. The correction could be made to within an accuracy of 100  $\mu\text{m}$ .

The performance of the SCIFI target system was investigated with 1.6-GeV/ $c$  minimum-ionizing  $\pi^+$ 's. The clusters of bright pixels were considered to be due to minimum-ionizing  $\pi^+$ 's, and the number of photo-electrons for the minimum-ionizing particle was

estimated to be 0.25/sheet from the number of clusters. The size of the clusters of a single photo-electron was  $11 \mu\text{m}$  on the CCD-chip and that at the input window of the I.I.T was  $120 \mu\text{m}$  (r.m.s.). The resolution of the SCIFI target system was determined to be  $300 \mu\text{m}$  from the distribution of the center of each cluster around the straight line.

### 3. Image data analysis

From the knowledge of the momenta of the incident  $\pi^+$ 's and outgoing  $K^+$ 's, missing masses were calculated. The events which fell between 1150 and 1250  $\text{MeV}/c^2$  in the missing mass spectrum were selected as  $\Sigma^+$ 's which were produced by the  $(\pi^+, K^+)$  reaction in the target, and their image data were fed to the automatic tracking program.

All experimental parameters such as various cuts, detection efficiencies, resolutions, etc., which were needed for the analysis below were obtained from a set of simulated image data described in Appendix A. In the simulation, all necessary experimental conditions such as I.I.T gains, photon conversion factors in the fiber, light transmission in the fiber, etc., were incorporated, and therefore the simulated data approximated the real data very closely. The simulated image data were then analyzed in exactly the same way as the real data to set the experimental parameters.

The analyzed simulated data using the cut parameters were then compared with the generated data as described in Appendix A. The efficiency due to a certain parameter setting was defined as the ratio of the number of the survived events to that of generated ones. For example, a threshold on brightness of tracks was set to define thick tracks and the efficiency was defined as the ratio of the number of tracks brighter than the threshold to the generated ones. The resolution of a certain parameter was defined as the width (FWHM or  $\sigma$ ) of the distribution of the parameter obtained from the analysis of the simulated data with respect to that of generated data. For instance, the resolution of the track length refers to the distribution of the analyzed track length relative to the generated track length. By applying the efficiency corrections, the life-time of  $\Sigma^+$  in the data was reproduced well as described in Appendix A.

The automatic tracking program finds particle tracks by the Hough transformation [9,10] which is a projection of a straight line to a point  $(\rho, \theta)$ , where the parameter  $\rho$  is the distance from a fixed point to the straight line, and  $\theta$  is the angle between the straight line and the  $Z$ -axis. Thus the points distributed around a line make a cluster in the  $(\rho, \theta)$  plane. Conversely, if a cluster is found in the  $(\rho, \theta)$  plane after the transformation, a straight line corresponding to the  $(\rho, \theta)$  value is recognized.

The tracks were divided into thick and thin tracks by setting a brightness cut on the pixel data before performing the Hough transformation. Among the thick tracks, those which intersected with two tracks corresponding to the incident  $\pi^+$  and outgoing  $K^+$  (identified by the beam line and spectrometer information) were retained for further analysis, as they define the vertices. The vertices obtained in each of the  $X$ - $Z$  and  $Y$ - $Z$  planes independently were compared to locate the  $Z$ -position. If the difference in the  $Z$ -positions of a vertex was less than 1.0 cm, then the thick track is considered to be a

$\Sigma^+$ , which must await further confirmation.

The  $\Sigma^+$  found above must show the signature of the decay and/or scattering before proceeding further. The former will be identified either by a thin branch ( $\pi^+$ ) or a thick branch (proton) from a thick track ( $\Sigma^+$ ), while the latter distinguishes itself by two thick branches ( $\Sigma^+$  and proton). In order to find one of the above branches of the found  $\Sigma^+$  track, we imposed a condition that one of the points needed to form another cluster in the  $(\rho, \theta)$  plane must belong to the found  $\Sigma^+$  track, which restricted the search only for the straight line intersecting the  $\Sigma^+$  track. That is, one of the points, which contribute to the cluster of the branch segment, must belong to the found  $\Sigma^+$  track. If the tracks of the branches on both planes were mutually consistent, the event was regarded as due to a  $\Sigma^+$ . An example of a typical event of the  $\Sigma^+$  production and decay which was recognized by the above algorithm is shown in Fig. 3.

Furthermore, a coplanarity condition of  $\pm 0.25$  rad was imposed on the  $\Sigma^+$  track, and the production angle for the reaction  $p(\pi^+, K^+)\Sigma^+$  had to be within  $\pm 0.25$  rad of the kinematical predicted angle. The background was reduced by 80% in the automatic tracking process.

A total of  $6 \times 10^4$  events were selected for further analysis by the automatic-tracking process with an efficiency of 47% for the  $\Sigma^+$  production and 64% for the  $\Sigma^+p$  scattering events. The efficiency increased dramatically to 80% and 90% for the  $\Sigma^+$  production and  $\Sigma^+p$  scattering, respectively, for those  $\Sigma^+$  tracks longer than 1.0 cm. The position resolution obtained from the program was 0.27 mm for the X- and Y-position, and 1.20 mm for the Z-position of the production position, and 0.50 mm for X-, 0.47 mm for the Y-, and 1.33 mm for the Z-position of the decay.

The events selected by the program were eye-scanned manually for the following event patterns:

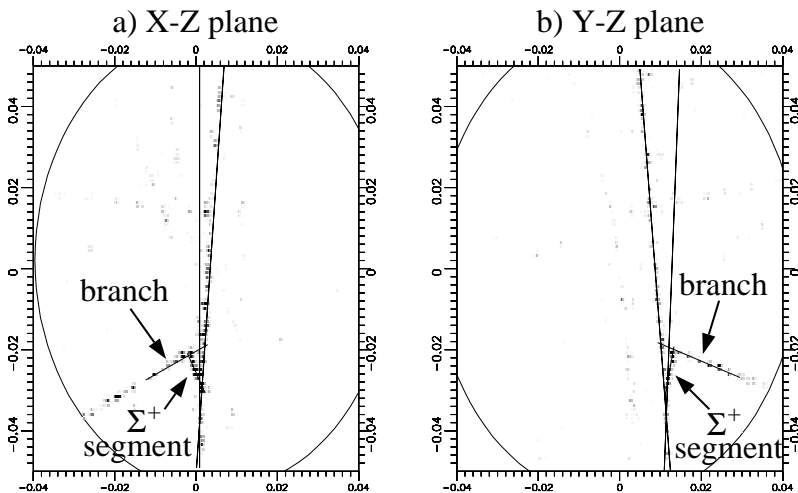


Fig. 3. An example of the result of the automatic-tracking process for the real image data. The images on (a) the X-Z plane and (b) the Y-Z plane are shown.

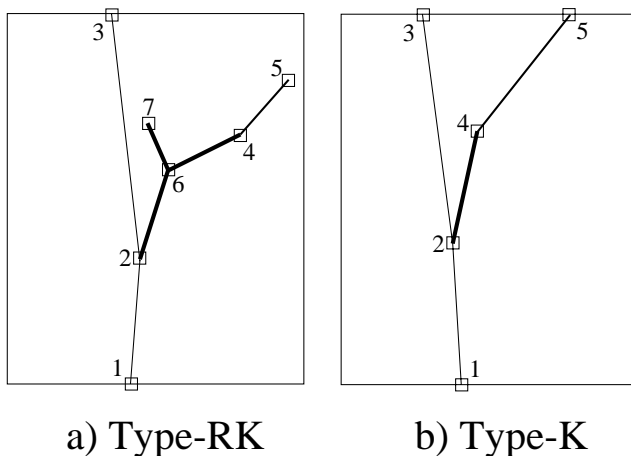


Fig. 4. Selected event patterns by eye-scanning. The open squares and the numbers in the pictures indicate respectively the recorded points and the pointing order of the eye-scanning process (see the text).

- (i) *Type-RK* The track of  $\Sigma^+$  candidate is associated with a recoil prong which is followed by a “kink” as shown in Fig. 4a. This is regarded as due to the  $\Sigma^+p$  scattering followed by decay of the scattered  $\Sigma^+$  particle.
- (ii) *Type-K* The track of  $\Sigma^+$  candidate with a “kink” as shown in Fig. 4b). This is due to the  $\Sigma^+$  production followed by decay.

Then points were identified visually on the video pictures as shown in Fig. 4. This process is termed “eye-scanning”.

In the eye-scanning process, the track length was determined by identifying the end-points on the video pictures which caused a systematic error of less than 1 mm, while overall position resolution was 1.2 mm in the track direction. The angular resolution is inversely proportional to the flight length, the proportionality constant being 0.79 mm. This means that the position resolution in the perpendicular direction to the track is 0.79 mm.

However, for very short tracks and/or small angles between the tracks, the event identification is ambiguous, and in order to avoid the ambiguity, such events in the eye-scanning process were not analyzed by setting threshold values in the track length and angle (visibility cut). The fiducial area in each of the  $X$ - $Z$  and  $Y$ - $Z$  planes was defined from the geometry of the target as the area of an ellipse with major axis of 9 cm in the beam direction and with minor axis of 7 cm for both planes. All the tracks analyzed must start and terminate within the ellipse.

The momentum of  $\Sigma^+$  for the H-like event (Appendix B) was determined uniquely from the momenta of the incident  $\pi^+$ , the outgoing  $K^+$ , and the direction of  $\Sigma^+$ . The  $\Sigma^+$  momentum of a C-like event was obtained from the kinetic energy of the proton from the  $\Sigma^+ \rightarrow p + \pi^0$  decay if it stopped in the fiducial area. For this purpose, the range–energy relation was used with more severe and stringent conditions for the visibility of the decay particle for the C-like event.

For K-type events, the threshold was set according to the production mechanism, i.e. if  $\Sigma^+$ 's were produced on hydrogen (H-like), it was set 6 mm for  $\Sigma^+$ 's, and 3 mm for decay tracks, while for those produced on carbon (C-like), 6 mm for the decay tracks was used. It was also imposed that the difference in the Z-coordinates between the starting and end points of the  $\Sigma^+$  track (both cases) and the decay particle (C-like) should be greater than 1 mm, since a track perpendicular to the Z-direction showed a broken line due to the alternating layer structure of the SCIFI target. For decay angles, the threshold was set at 0.2 rad. The perpendicular distances from the decay point to the outgoing  $K^+$  track which were longer than 1 mm were analyzed in order to avoid the overlap of tracks.

For RK-type of events, the thresholds for  $\Sigma^+$  tracks before and after scattering were set at 4 mm with recoil proton tracks longer than 3 mm. Position difference in the Z-direction of  $\Sigma^+$  track before and after scattering and that of recoil proton track were required to be larger than 1 mm. The decay angle was required to be larger than 0.1 rad. The perpendicular distances from the decay point to the recoil proton track, and to the  $\Sigma^+$  track before scattering, those from the scattering point to the outgoing  $K^+$  track, those from the end point of the recoil proton to the  $\Sigma^+$  track after scattering which were longer than 1 mm were analyzed. All scattering events were classified by the kinematic fitting according to (a) the H-like  $\Sigma^+$ 's scattering on hydrogen, (b) the C-like  $\Sigma^+$  scattering on hydrogen.

The kinematics of  $\Sigma^+p$  scattering requires the momenta of  $\Sigma^+$  before and after scattering as well as that of the recoil protons. The momentum resolution of the  $\Sigma^+$  differs depending on the  $\Sigma^+$  production: (a) for H-like events,  $\Delta p/p = 19 \text{ MeV}/c$ , (b) for C-like events,  $\Delta p/p = 51 \text{ MeV}/c$ . Correspondingly, the resolution of the scattering angle in the C.M. system, was  $\Delta(\cos \theta_{\text{CM}}) = 0.09$  in the case of (a), and 0.15 in the case of (b).

The total number of  $\Sigma^+$ -production events was obtained from the K-type events and that of  $\Sigma^+p$  scattering events from the RK-type. The  $\Sigma^+p$  scattering cross section can be obtained from these two numbers.

#### 4. The cross section and errors

The number of events which were finally identified as  $\Sigma^+p$  scattering was 11. The production target nuclei, track lengths of the  $\Sigma^+$  before and after scattering, and the recoil proton for these events are listed in Table 1. From these the particle momenta were obtained at the scattering points and the scattering angles in the center-of-mass system. The pictures of a typical event in the SCIFI target are shown in Fig. 5.

In the analysis, only those events with two branches corresponding to the  $\Sigma^+$  and the recoil proton tracks visible at the scattering point were included. Some events due to  $C(\Sigma^+, \Sigma^+p)X$  quasi-free knockout reaction could contribute to  $\Sigma^+p$  scattering as background, if the recoil nucleus in the above reaction leaves no measurable track. The number of such background events can be estimated from the known cross section of the

Table 1

List of  $\Sigma^+p$  scattering events. “H” in production target means H-like  $\Sigma^+$ -production events and “C” means C-like events

Run–Spill–Event	Production target	$\Sigma^+$ before scattering (mm)	$\Sigma^+$ after scattering (mm)	Recoil proton (mm)	Momentum (MeV/c)	Scattering angle $\cos\theta_{CM}$
430–3143–01	C	17.0	4.4	7.8	352	−0.116
449–2894–12	C	5.2	35.8	34.8	506	0.066
451–0503–04	C	11.2	6.5	6.0	413	0.246
462–3343–07	C	10.7	8.5	7.6	430	0.214
465–1484–12	H	13.2	4.3	8.2	415	0.176
506–2907–03	C	26.5	6.6	21.4	477	−0.072
517–2799–07	C	12.6	7.4	4.0	314	0.112
533–2304–02	C	6.0	15.5	6.6	448	0.364
539–0819–03	H	4.5	18.9	9.0	419	0.131
555–1674–03	C	21.7	5.7	5.0	468	0.555
569–0567–13	H	6.3	4.4	4.1	475	0.545

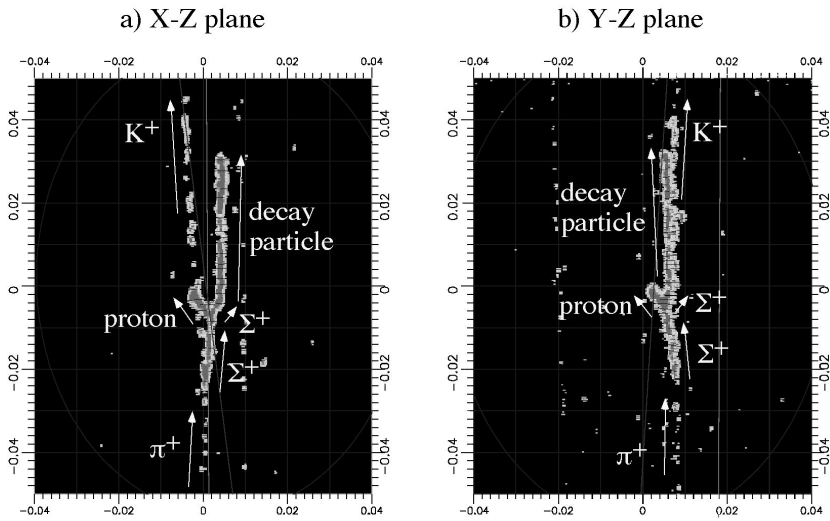


Fig. 5. Pictures of a typical event finally identified as  $\Sigma^+p$  scattering. The images on (a) the X–Z plane and (b) the Y–Z plane are shown.

reaction  $^{12}\text{C}(p, 2p)^{11}\text{B}$  at the incident proton of 644 MeV/c [11]. The estimate shows that the cross section of the reaction  $^{12}\text{C}(p, 2p)^{11}\text{B}$  is 20–60% of the free  $p$ – $p$  scattering cross section at the same momentum. However, these quasi-free events were reduced significantly in the kinematic-fitting process, and it is estimated that the background due to  $\Sigma^+$ –C scattering in the present data is 8–22%.

The event topology of  $\Sigma^+p$  scattering is composed of a recoil proton prong and the  $\Sigma^+$  decay. The latter is also used to obtain the number of  $\Sigma^+$ 's. Thus, we expect that the systematic errors in identifying the topology of the  $\Sigma^+$  decay almost cancel out, but the errors due to the proton identification in the scattering topology remain.

The largest systematic uncertainty came from the process of locating the points of interest on the video pictures as stated earlier. The systematic errors were determined by adding and subtracting 1 mm in the topology of  $\Sigma^+$  decay to be  $\pm 16\%$ , and those in the topology of  $\Sigma^+$  scattering and its decay to be  $\pm 24\%$ . The error in the cross section, however, was  $\pm 14\%$  due to the partial cancellation effect mentioned above, and the total systematic error was estimated to be  $\pm 16\%$ .

The  $\Sigma^+p$  scattering events were divided into two regions of scattering angle in the center-of-mass system, i.e.  $-0.4 \leq \cos \theta_{\text{CM}} < 0.1$  and  $0.1 \leq \cos \theta_{\text{CM}} < 0.6$ , and the differential cross sections for  $\Sigma^+p$  scattering in the incident momentum region from 300 to 600 MeV/c are obtained at these two angles.

$$\frac{d\sigma}{d\Omega} = \begin{cases} 2.1^{+3.2}_{-1.1} \text{ (mb/sr)} & (-0.4 \leq \cos \theta_{\text{CM}} < 0.1) \\ 3.1^{+2.1}_{-1.2} \text{ (mb/sr)} & (0.1 \leq \cos \theta_{\text{CM}} < 0.6) \end{cases}$$

These errors are statistical ones, which include errors in the real data and the ambiguity of the efficiency given by the statistics of the simulated image data. The error in the small number of events corresponds to a probability of 68.3% for the Poisson distribution, which makes the statistical errors asymmetric. In addition, there is also an additional overall systematic error of  $\pm 16\%$  mentioned above.

## 5. Discussion

In the present experiment, two points in the differential cross sections for  $\Sigma^+p$  scattering are measured in the momentum region where no such data have been obtained previously. The obtained values are displayed in Fig. 6 together with those calculated by the Nijmegen group [12] and the Kyoto–Niigata group [13], while the phase shifts for the triplet  $^3S_1$  and singlet  $^1P_1$  waves are shown in Table 2.

The Nijmegen group proposes models based on OBE picture with a phenomenological core for a short-range repulsive force. For the hard-core model, HC-D and HC-F, an

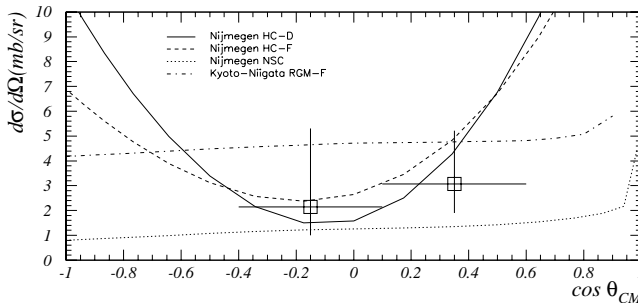


Fig. 6. Comparison of the measured differential cross sections for  $\Sigma^+p \rightarrow \Sigma^+p$  with theoretical calculations by the Nijmegen group with the hard-core models D (HC-D), F (HC-F), and the soft-core model (NSC) [12] and by the Kyoto–Niigata group with the quark-cluster model (RGM-F) [13] at the  $\Sigma^+$  momentum of 400 MeV/c.

Table 2  
Phase shifts of  $\Sigma^+p$  scattering at 400 MeV/c

Model	Nijmegen			Kyoto–Niigata
	HC-D	HC-F	NSC	RGM-F
$^3S_1$ wave (degree)	–17.20	–28.14	–10.46	–36.40
$^1P_1$ wave (degree)	52.25	39.62	4.27	4.87

infinitely large potential at the short distances is used, whereas a Gaussian-type potential to account for the exchange of the Regge trajectories is used in the soft-core model (NSC). The calculated cross sections by the Nijmegen group with the hard-core models show a quadratic behavior in  $\cos\theta$  which originates from the large contribution from the  $^1P_1$  wave. On the other hand, the cross section in the soft-core model is almost isotropic because of smaller contribution of the  $^1P_1$  wave.

The Kyoto–Niigata group model, RGM-F, is a QCM based on the RGM in the short range. In this model the contribution of the  $^1P_1$  wave is small and the differential cross section does not show a quadratic behavior. The total cross section is larger than those of Nijmegen models because of larger phase shift in the  $^3S_1$  wave as shown in Table 2. The measured cross section are consistent with the predictions of the Nijmegen hard-core models as well as the Kyoto–Niigata quark-cluster model within the statistical errors. The present results appear to favor less the prediction of the Nijmegen soft-core model, although the statistics are not sufficient to draw definitive conclusions.

As for this scintillating fiber technique, several improvements will be possible. The spatial resolution can be improved by using thinner scintillating fiber. The cross section of a fiber may be changed down to about a  $250\ \mu\text{m} \times 250\ \mu\text{m}$  square which corresponds to a pixel size of the CCD under the present magnification factor, so that the threshold of the length of tracks in the image analysis could be shortened by a factor of 60–70%, e.g. from 4 mm to 2.5 mm. Then, the angular region will be extended to  $-0.6 \leq \cos\theta_{\text{CM}} < 0.7$  (from  $-0.4 \leq \cos\theta_{\text{CM}} < 0.6$  of this experiment which is limited by the threshold of the length of recoil proton tracks). The coverage of the scattering angle is of vital importance to check the theoretical models, since the angular distribution of this  $\Sigma^+p$  scattering is quite sensitive to the contribution of the  $^1P_1$  partial wave, especially at forward and backward angles as shown in Fig. 6.

This technique can also be applied to measure other channels such as  $\Sigma^-p$  scattering via the  $(\pi^-, K^+)$  or  $(K^-, \pi^+)$  reactions and  $\Lambda p$  scattering via the  $(\pi^+, K^+)$  reaction. Furthermore, the polarization of scattered  $\Sigma^+$  or  $\Lambda$  can be measured, since the decay asymmetry of these hyperons can be observed in the SCIFI detector. Such data would be quite effective in discriminating between various models, since the predictions by the models mentioned above are significantly different [14].

Similar detector systems, consisting of SCIFI and CCD, are also used to detect decay products from double-strangeness nuclei and/or H-dibaryon at BNL [15] and KEK [16]. At the BNL experiment, beam intensity was one order of magnitude higher.

However, the present rate of this technique is limited by the decay constant of the phosphor in the first stage of the I.I.T. If one incorporates a fast imaging device such as a gateable image pipeline [17] as a device in the first stage instead of an image intensifier in future experiments, beam intensity up to  $10^7$  Hz will be acceptable. More than one order of magnitude improvement in statistics would be available in this case.

## Acknowledgements

The analysis of the visual image data from the SCIFI-target system was expedited greatly by the use of the Hough transformation, which was suggested by Professor A. Ono, to whom we express our special thanks. The dedication and support of many of the KEK staff during the experiment and analyses are very much indebted. We thank Professors H. Sugawara, K. Nakai and T. Ohshima for their continuous encouragement throughout this work. We express our sincere appreciation to Professors T. Sato and Y. Yoshimura for the inspiring information on bubble chamber experiments. The theoretical calculations for  $\Sigma^+p$  elastic scattering were provided by Professor A. Rijken for the Nijmegen model, and Professor Y. Fujiwara for the Kyoto–Niigata model. Helpful discussions with Professors A.A. Cowley, T. Noro, H. Sakaguchi and M. Yosoi on the evaluation of the  $\Sigma^+$ –carbon scattering cross section were much appreciated. The experiment was supported in part by a Grant-in-Aid for Scientific Research (02402008, 06640425), the Ministry of Education, Science and Culture in Japan, the Korea Science and Engineering Foundation, and the Basic Science Research Institute Program (BSRI-96-2408), Ministry of Education, Republic of Korea.

## Appendix A. Image data simulation

A Monte Carlo simulation to produce a set of dummy image data was performed using the GEANT 3.15 package [18]. Two sets of dummy image data were generated, one for the  $\Sigma^+$  production and the other for the  $\Sigma^+$  production followed by scattering on hydrogen. The incident momentum of the  $\pi^+$  beam was set at 1.64 GeV/ $c$  with a momentum spread of 14 MeV/ $c$  (standard deviation).

The  $\Sigma^+$  production from the reaction  $p(\pi^+, K^+)\Sigma^+$  and that from the  $C(\pi^+, K^+)\Sigma^+$  reaction were simulated. The cross section and angular distribution of the reaction  $p(\pi^+, K^+)\Sigma^+$  given in Ref. [19] were used for this purpose. In the case of the reaction  $C(\pi^+, K^+)\Sigma^+$ , a quasi-free  $\Sigma^+$  production via the  $\pi^+ + (p) \rightarrow K^+ + \Sigma^+$  reaction in carbon was used by assuming that the proton momentum distribution due to the Fermi motion is given by

$$N(p) = \frac{N_0}{1 + \exp\left(\frac{p \text{ (GeV}/c) - 0.1}{0.05}\right)}.$$

Energy losses of particles in each scintillating fiber obtained with the GEANT code was converted to the number of photons in scintillating fibers, the distribution of which was assumed to be uniform over the cross-sectional area of a scintillating fiber ( $500 \mu\text{m} \times 500 \mu\text{m}$ ) at the I.I.T. surface. The position of photons was spread out further by  $200 \mu\text{m}$  to take care of the misalignment of the SCIFI stack and the intrinsic resolution of the I.I.T. system.

Photo-electrons produced on the photo-cathode of I.I.T. were assumed to obey a Poisson distribution with an average number of electrons of six per MeV. The amplification of photo-electrons in the I.I.T. was adjusted to have a total brightness in FADC of  $55 \pm 15$  per photo-electron. Finally, a Gaussian distribution with a width of  $250 \mu\text{m}$  was assumed for the photons on the CCD pixels.

A test of the efficiency correction was performed by reproducing the life-time of  $\Sigma^+$  in the data. The result was  $c\tau = 2.38 \pm 0.24$  cm, which agreed with the known value [20],  $c\tau = 2.396 \pm 0.012$  cm. It should be noted that the efficiency corrections applied here include those for all the processes needed to evaluate the cross section, i.e. efficiencies for the automatic tracking, the eye-scanning, the brightness requirement, and the kinematic fitting.

## Appendix B. Kinematic fitting

The  $\Sigma^+$ -production events were categorized into H-like and C-like events according to whether the observed variables satisfy the kinematics of the  $\Sigma^+$  production on hydrogen. The kinematic constraints were expressed by the following equation based on the energy-momentum conservation:

$$C_1 = p_\pi \sin \theta_\pi \cos \phi_\pi - p_K \sin \theta_K \cos \phi_K - p_\Sigma \sin \theta_\Sigma \cos \phi_\Sigma,$$

$$C_2 = p_\pi \sin \theta_\pi \sin \phi_\pi - p_K \sin \theta_K \sin \phi_K - p_\Sigma \sin \theta_\Sigma \sin \phi_\Sigma,$$

$$C_3 = p_\pi \cos \theta_\pi - p_K \cos \theta_K - p_\Sigma \cos \theta_\Sigma,$$

$$C_4 = E_\pi + m_p - E_K - E_\Sigma,$$

$$C_5 = E_\pi^2 - p_\pi^2 - m_\pi^2,$$

$$C_6 = E_K^2 - p_K^2 - m_K^2,$$

$$C_7 = E_\Sigma^2 - p_\Sigma^2 - m_\Sigma^2,$$

where ten observed variables,  $o_i$  ( $i = 1, \dots, 10$ ), are  $E_\pi$ ,  $E_K$ ,  $p_\pi$ ,  $p_K$ ,  $\theta_\pi$ ,  $\theta_K$ ,  $\theta_\Sigma$ ,  $\phi_\pi$ ,  $\phi_K$  and  $\phi_\Sigma$ , and two unobserved variables,  $u_k$  ( $k = 1, 2$ ), are  $E_\Sigma$  and  $p_\Sigma$ .

$E_\pi$ ,  $E_K$  and  $E_\Sigma$  are energies and  $p_\pi$ ,  $p_K$  and  $p_\Sigma$  are momenta of the incident  $\pi^+$ , outgoing  $K^+$  and produced  $\Sigma^+$ , respectively. The  $\theta$ 's and  $\phi$ 's are the dip angles and azimuthal angles for the tracks indicated by the subscripts respectively. The masses of the particles are denoted as  $m_\pi$ ,  $m_K$ , and  $m_\Sigma$ .

The kinematic fitting procedure is a method to obtain the best fit within the kinematic constraints. The constraints  $C_j$ 's ( $j = 1, \dots, 7$ ) should be zero ideally. The  $C_j$ 's,

however, are not zero in the real experimental data since the observed variables have experimental errors. The functions to be minimized are  $S = G_{il} a_i a_l$ , where  $a_i = o_i - f_i$ . The  $f_i$ 's ( $i = 1, \dots, 10$ ) are the fit parameters of the observed variables  $o_i$ . The  $G_{il}$  is the inverse error matrix of the observed variables, which include the momentum, position and angle resolutions mentioned in the text. The function  $S$  was minimized using the Lagrange multiplier method [21].

The fitted momenta from the simulated data were compared with those used in generating the simulated data, and yielded  $\Delta p \simeq 12 \text{ MeV}/c$  for the  $\Sigma^+$  production on hydrogen and  $\Delta p \simeq 43 \text{ MeV}/c$  for that on carbon. The poorer resolution for the  $\Sigma^+$  production on carbon arises from the limited resolution of the decay angle. If  $\Sigma^+$ 's produced on carbon were misidentified as H-like events, the momentum resolution of the H-like events obtained by the kinematic fitting would be poorer than the one for real H-like events.

## References

- [1] R. Engelmann et al., Phys. Lett. 21 (1966) 587;  
G. Alexander et al., Phys. Rev. 173 (1968) 1452;  
B. Sechi-Zorn et al., Phys. Rev. 175 (1968) 1735;  
G.R. Charlton et al., Phys. Lett. B 32 (1970) 720;  
J.A. Kadyk et al., Nucl. Phys. B 27 (1971) 13;  
F. Eisele et al., Phys. Lett. B 37 (1971) 204;  
J.M. Hauptman et al., Nucl. Phys. B 125 (1977) 29.
- [2] M.M. Nagels, Th.A. Rijken and J.J. de Swart, Phys. Rev. D 15 (1977) 2547; D 20 (1979) 1633;  
P.M.M. Maessen, Th.A. Rijken and J.J. de Swart, Phys. Rev. C 40 (1989) 2226.
- [3] B. Holzenkamp, K. Holinde and J. Speth, Nucl. Phys. A 500 (1989) 485;  
A. Reuber, K. Holinde and J. Speth, Nucl. Phys. A 570 (1994) 543.
- [4] M. Oka and K. Yazaki, in Quarks and Nuclei, ed. W. Weise (World Scientific, Singapore, 1984) p. 489;  
K. Yazaki, in Perspectives of Meson Science, ed. Yamazaki, K. Nakai, K. Nagamine (Elsevier Science Publishers, Amsterdam, 1992) p. 795.
- [5] U. Straub, Z.Y. Zhang, K. Bräuer, A. Faessler, S.B. Khadkikar and G. Lübeck, Nucl. Phys. A 483 (1988) 686; A 508 (1990) 385c.
- [6] C. Nakamoto, Y. Suzuki and Y. Fujiwara, Prog. Theor. Phys. 94 (1995) 65;  
Y. Fujiwara, C. Nakamoto and Y. Suzuki, Prog. Theor. Phys. 94 (1995) 215, 353; Phys. Rev. Lett. 76 (1996) 2242.
- [7] J.K. Ahn et al., Phys. Lett. B 378 (1996) 53;  
Y. Goto, Ph.D. thesis, Kyoto Univ. (Memoirs of the Faculty of Science, Kyoto University, (Series of Physics, Astrophysics, Geophysics and Chemistry) Vol. 40-1 (1997) 1);  
S. Yamashita, Ph.D. thesis, Kyoto Univ. (Memoirs of the Faculty of Science, Kyoto University, (Series of Physics, Astrophysics, Geophysics and Chemistry) Vol. 39-3 (1996) 349);  
Y. Itow, Ph.D. thesis, Kyoto Univ. (Memoirs of the Faculty of Science, Kyoto University, (Series of Physics, Astrophysics, Geophysics and Chemistry) Vol. 39-3 (1996) 397).
- [8] Manufactured by KURARAY Co. Ltd., Tokyo 103-0027, Japan.
- [9] A. Ono, private communications.
- [10] J. Illingworth and J. Kittler, Computer Vision, Graphics, and Image Processing 44 (1988) 87.
- [11] A.A. Cowley, J.V. Pilcher, J.J. Lawrie and D.M. Whittall, Phys. Rev. C 40 (1989) 1950.
- [12] Th.A. Rijken, private communication. See also Refs. [2].
- [13] Y. Fujiwara, C. Nakamoto, private communication. See also Ref. [6].
- [14] Th.A. Rijken, P.M.M. Maessen and J.J. de Swart, Nucl. Phys. A 547 (1992) 245c;  
K. Holinde, Nucl. Phys. A 547 (1992) 255c.

- [15] BNL-AGS Experiment 885, Search for Double Dambda Hypernuclei using Scintillating Fiber Arrays and Neutron Detectors, spokes persons: M. May, G Franklin, C.A. Davis, unpublished.
- [16] KEK-PS Experiment 373, Study of  $S = -2$  Nuclei by Emulsion-Scintillating Fiber Hybrid Method, spokes person: K. Nakazawa, unpublished.
- [17] A.G. Berkovski et al., Nucl. Instrum. Meth., A 380 (1996) 537.
- [18] GEANT – Detector Description and Simulation Tool, CERN Program Library Long Writeup W5013 (1993).
- [19] D.J. Candlin et al., Nucl. Phys. B 226 (1983) 1.
- [20] Review of Particle Physics, Eur. Phys. J. C 3 (1998) 1.
- [21] L. Lyons, Statistics for Nuclear and Particle Physicists (Cambridge Univ. Press, Cambridge, 1986).